ARTICLES
PUBLISHED ONLINE: 1 DECEMBER 2014 | DOI: 10.1038/NNANO.2014.277

nature nanotechnology

A silicon-based photocathode for water reduction with an epitaxial $SrTiO_3$ protection layer and a nanostructured catalyst

Li Ji[1,2]*, Martin D. McDaniel[3], Shijun Wang[2], Agham B. Posadas[4], Xiaohan Li[1], Haiyu Huang[1], Jack C. Lee[1], Alexander A. Demkov[4], Allen J. Bard[2], John G. Ekerdt[3] and Edward T. Yu[1]

The rapidly increasing global demand for energy combined with the environmental impact of fossil fuels has spurred the search for alternative sources of clean energy. One promising approach is to convert solar energy into hydrogen fuel using photoelectrochemical cells. However, the semiconducting photoelectrodes used in these cells typically have low efficiencies and/or stabilities. Here we show that a silicon-based photocathode with a capping epitaxial oxide layer can provide efficient and stable hydrogen production from water. In particular, a thin epitaxial layer of strontium titanate ($SrTiO_3$) was grown directly on Si(001) by molecular beam epitaxy. Photogenerated electrons can be transported easily through this layer because of the conduction-band alignment and lattice match between single-crystalline $SrTiO_3$ and silicon. The approach was used to create a metal–insulator–semiconductor photocathode that, under a broad-spectrum illumination at 100 mW cm^{-2}, exhibits a maximum photocurrent density of 35 mA cm^{-2} and an open circuit potential of 450 mV; there was no observable decrease in performance after 35 hours of operation in 0.5 M H_2SO_4. The performance of the photocathode was also found to be highly dependent on the size and spacing of the structured metal catalyst. Therefore, mesh-like Ti/Pt nanostructured catalysts were created using a nanosphere lithography lift-off process and an applied-bias photon-to-current efficiency of 4.9% was achieved.

Since Honda and Fujishima's pioneering work on electrochemical photolysis of water using TiO_2 in 1972[1], much effort has been put into this area as it provides a way to convert solar energy into a storable clean fuel. In designing photoelectrochemical (PEC) cells, a fast charge transfer at the semiconductor/aqueous interface, long-term stability and efficient harvesting of a large portion of the solar spectrum are three key priorities[2]. Based on this, many material systems have been studied, including Si[3–13], various metal oxides[14–20], III–V semiconductors[21] and others[22–24]. High efficiencies have been achieved in triple-junction amorphous Si or III–V semiconductors, but at high cost and device complexity[10,21]. For metal oxides, large bandgaps (usually larger than 2 eV) limit their light absorption, which makes them inefficient for solar-energy conversion. Si, a semiconductor with a narrow bandgap (1.1 eV), is capable of absorbing a much larger portion of the solar spectrum and has already been widely used in the photovoltaic industry[25,26]. However, Si is not stable in aqueous conditions. Therefore, a corrosion-resistant protective layer that does not inhibit the transfer of photogenerated carriers (electrons or holes) is highly desirable.

Many materials have been studied as protective layers on Si[3–9,27–31]. The relatively low efficiencies reported in these works result from the difficulty in achieving a high-quality Si/metal or Si/metal-oxide junction without a disordered SiO_x or silicide layer. Recently, a significant improvement in the performance of Si-based photoelectrodes was demonstrated successfully with the growth of a high-quality thermal SiO_2 tunnel layer[3]. However, the large conduction-band offset between SiO_2 and Si creates a larger electron tunnelling barrier, which inhibits the charge transport through the junction.

A protective layer with minimal band offset and a high-quality interface is necessary to maximize the efficiency of Si-based photoelectrodes. Strontium titanate, $SrTiO_3$ (STO), is one of the few oxides that can be grown epitaxially on Si(001) with minimal interfacial reactions[32–35]. The lattice constant of a cubic perovskite STO (3.905 Å) matches well with the Si(001) surface unit cell (3.84 Å), and results in a small (−1.7%) lattice mismatch with the STO compressively strained to Si. Crystalline STO can be grown on Si with a very low interface state density, which creates a nearly perfect electrical interface[36]. In addition, the conduction-band alignment of the STO/Si heterojunction has been explored, both experimentally and theoretically, and found to be near zero[37–41]. Electron transport from the Si substrate through the STO layer is facilitated because of this minimal conduction-band offset. In this work, a thin epitaxial STO layer is grown directly on Si(001) to provide a stable Si-based photocathode for efficient PEC water splitting. Furthermore, we found that the use of nanostructured surface metal catalysts, which we fabricated using a nanosphere lithography-patterning process, greatly enhances the efficiency.

Crystalline structure and interface quality

Single-crystal STO is grown on Si(001) by molecular beam epitaxy (MBE) using a variant of the Motorola-developed process[42]. More detailed information of the growth is given in the Methods section. The crystalline structure of the STO protective layer grown on Si(001) was confirmed by reflection high-energy electron diffraction (RHEED). RHEED images for a STO-film thickness of four unit cells (~1.6 nm) grown by MBE are shown in Fig. 1a,b. The RHEED images are taken along the [110] and [210] azimuth

---

[1] Microelectronics Research Center, Department of Electrical and Computer Engineering, University of Texas at Austin, Texas 78712, USA. [2] Center for Electrochemistry, Department of Chemistry and Biochemistry, University of Texas at Austin, Texas 78712, USA. [3] Department of Chemical Engineering, University of Texas at Austin, Texas 78712, USA. [4] Department of Physics, University of Texas at Austin, Texas 78712, USA. *e-mail: nmgjili@utexas.edu

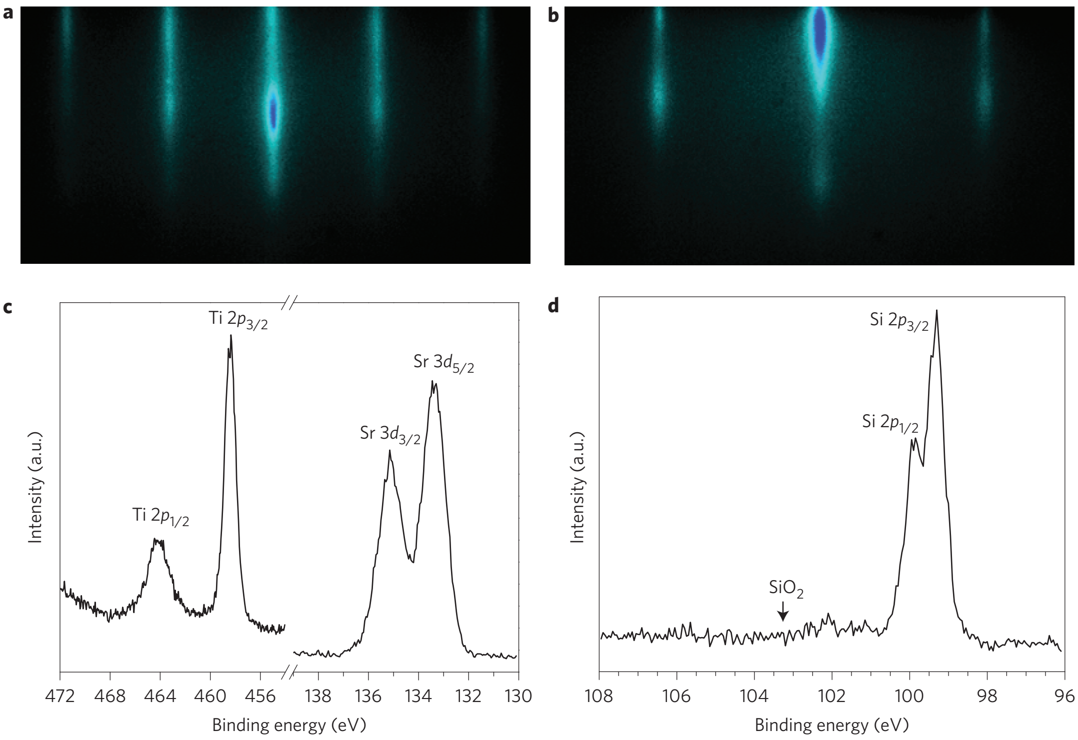

Figure 1 | RHEED and XPS results. a,**b**, RHEED images of a STO film of thickness four unit cells (1.6 nm) grown by MBE on p-Si(001). The beam is aligned along the [110] and [210] azimuth for **a** and **b**, respectively. **c**,**d**, High-resolution X-ray photoelectron spectra of a STO film of thickness eight unit cells (3.1 nm) that shows the Sr 3*d* and Ti 2*p* core levels (**c**), and the Si 2*p* core level (**d**), which confirm that negligible SiO_2 is present at the STO–Si interface.

of the cubic perovskite. The elongated streak patterns indicate a well-crystallized and atomically smooth film. Rotation of the sample under electron illumination confirmed the four-fold symmetry and registry with the underlying Si substrate.

Film composition and quality of the STO–Si interface were analysed using *in situ* X-ray photoelectron spectroscopy (XPS). The STO-film composition was shown to be stoichiometric (50%) to slightly Sr rich (52%) for thicknesses of 4–10 unit cells (1.6–4 nm). Figure 1c shows high-resolution XPS spectra of the Sr 3*d* and Ti 2*p* core levels. The positions of the binding-energy peaks of the Sr $3d_{5/2}$ (133.5 eV) and Ti $2p_{3/2}$ (458.4 eV) are consistent with those of fully oxidized species (Sr^{2+} and Ti^{4+}) found in bulk single-crystal STO.

Figure 1d shows the Si 2*p* core level after the deposition of a STO-film thickness of eight unit cells (3.1 nm). The absence of a peak at ~103.3 eV suggests that the interface is nearly free of amorphous SiO_2; however, a small presence of suboxide (SiO_x) or silicate is observed at a slightly lower binding energy (~102 eV). Nevertheless, the STO film is of high crystalline quality with a reasonably abrupt STO–Si interface. This provides an ideal material system for electron transport from the Si substrate to the STO surface.

Thickness dependence and conducting mechanism

Figure 2a shows a schematic diagram of the STO/p-Si photocathode. Incident light travels through the ultrathin STO layer and is absorbed predominantly by the Si substrate. Photogenerated electrons then travel across the STO layer to the Ti/Pt metallic catalyst, at which H_2 is produced. As indicated in Fig. 2b, electron transport across the STO is facilitated by the small conduction-band offset. Prior studies have shown that work-function engineering using a Ti/Pt bilayer further improves catalyst performance[3]. The Ti/Pt bilayer structure was used for two reasons. First, the adhesion of Pt directly to the STO surface was weak. After several minutes of PEC operation, Pt came off the STO surface and the performance degraded significantly. Inserting a Ti layer improved the adhesion and solved this problem. Second, in metal–insulator–semiconductor (MIS) PEC cells, the metal serves as the catalyst and simultaneously forms a Schottky junction. The open circuit voltage (V_{oc}) obtained in MIS junctions depends on the work-function difference between the metal and semiconductor. Although Pt is a good catalyst, its work function is large and comparable to that of p-Si, which results in a small V_{oc}. By inserting a Ti layer underneath Pt, the roles of the metal in determining V_{oc} and as a catalyst are decoupled, with Pt serving as the catalyst and Ti forming the MIS junction. Samples with Ti layers of different thicknesses (8 nm and 30 nm) were made and detailed results are shown in Supplementary Fig. 1.

To confirm the design principle that the solid-state properties of the oxide and its interface affect the PEC performance, linear sweep voltammetry (LSV) measurements were conducted in 0.5 M H_2SO_4 deaerated by Ar gas without any sacrificial reagent. A xenon arc lamp was used as the light source and the light intensity was calibrated to 100 mW cm^{-2} by a Si photodiode. Pt wire and Ag/AgCl were used as the counter electrode and reference electrode, respectively. Before testing the MIS photocathodes, a Pt wire was used as the working electrode and LSV was performed to calibrate the normal hydrogen electrode (NHE), illustrated as the grey line in Fig. 2c. LSV provides information on both the metal–electrolyte interface and the MIS junction. For the metal–electrolyte interface, a fast charge transfer is required. In Supplementary Fig. 2, STO/p-Si without a metal catalyst is seen to exhibit no photocurrent under a −0.8 V bias versus NHE, which indicates a low charge-transfer rate at the STO/electrolyte interface. By comparison, MIS photocathodes show great improvement in both photocurrent density and onset potentials, demonstrating the need for an appropriate metal catalyst.

For an MIS junction, the quality of the oxide layer impacts the photocurrent density, onset potential and transient behaviour. Thus, a key advantage of STO as the protection layer is the minimal conduction-band offset with Si, as shown in Fig. 2b. This can be demonstrated by performing current–voltage (*I*–*V*)

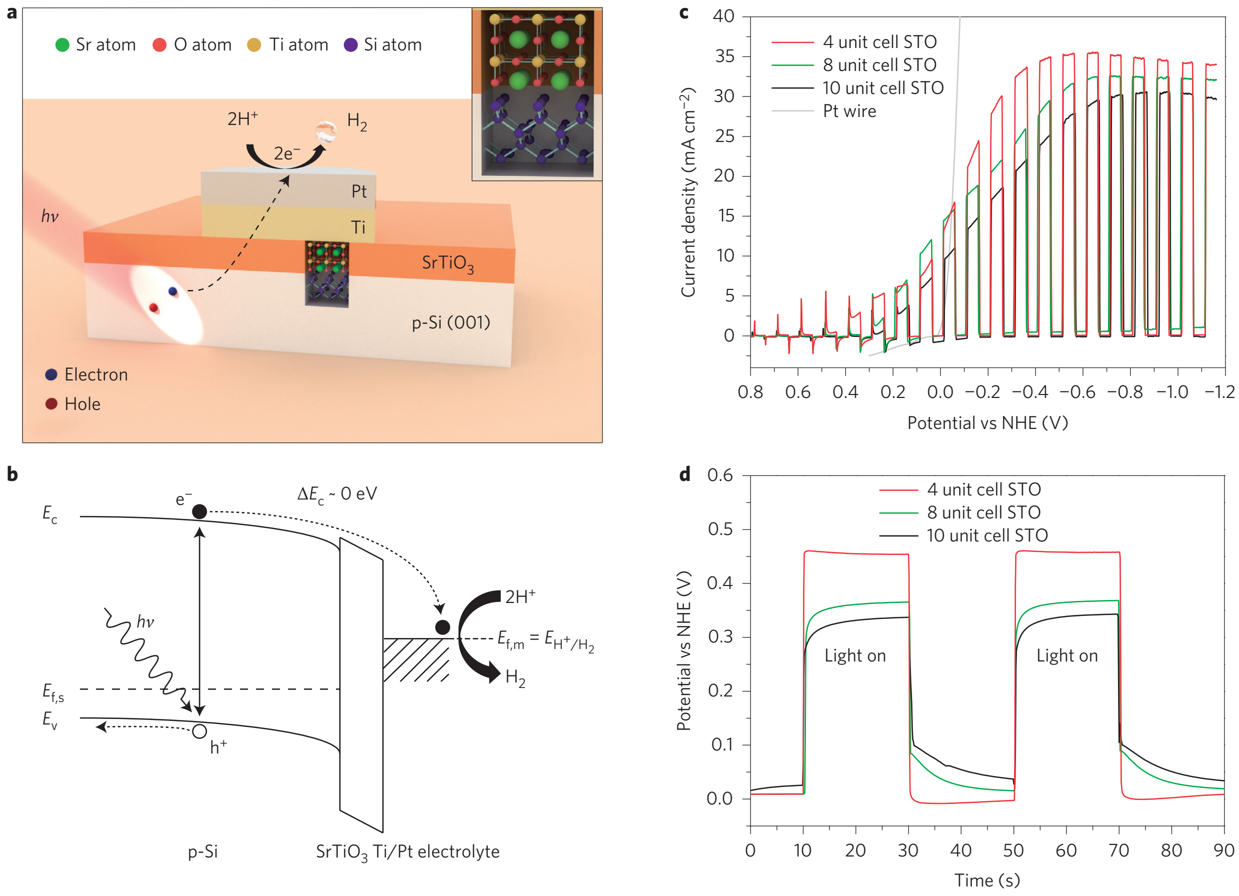

Figure 2 | Schematic structure, band alignment and STO-thickness-dependent performance. a, Schematic structure of the STO-protected Si photocathode shows that light is absorbed by the p-Si substrate and the photogenerated electrons tunnel to the surface metallic dots, at which H_2 is produced. The inset plot represents the interface between STO and Si(001), with a good lattice match. **b**, The energy-band diagram shows carrier generation and transport with a negligible conduction-band offset between STO and Si, which facilitates electron transport across the STO protection layer. E_c, E_v, $E_{f,s}$ and $E_{f,m}$ are the conduction band, valance band, Fermi level of silicon and metal, respectively. **c**,**d**, LSV (**c**) and open-circuit potential (**d**) measurements with chopped illumination for 20 nm Pt/30 nm Ti/STO/p-Si(001) for various STO thicknesses from four to ten unit cells. The sweep rate for LSV was 50 mV s^{-1}. The catalyst structures consisted of Pt/Ti dots 60 μm in diameter arranged in a square array with a 75 μm period.

measurements at various temperatures in a rough vacuum and a normalized conductance analysis. As shown in Supplementary Fig. 3, the I–V is temperature dependent and the normalized conductance is fixed at one, which confirms the band conduction as expected. As shown in Fig. 2c, the photocurrent density of the four-unit-cell STO sample reaches as high as 35 mA cm^{-2}, the highest limiting photocurrent reported for Si-based photoelectrodes[3–13]. This is attributed to the small conduction-band offset and single-crystalline nature and epitaxial interface of MBE-grown STO on Si, which facilitates electron transport and reduces recombination at the Si/STO interface. Recombination peaks are often observed during the transient state when switching the light on/off under a bias greater than the onset potential. However, as illustrated in Fig. 2c, all the single-crystalline STO samples exhibit no recombination peaks, which further indicates an excellent metal–oxide interface quality and a low concentration of interface traps and defects that can serve as recombination centres for photogenerated electron–hole pairs.

The onset potential shift for the STO sample of four unit cells obtained from the LSV results shown in Fig. 2c is 460 mV. To confirm this, the open-circuit potential versus time was measured. The onset potential shifts for samples of four, eight and ten unit cells are 450 mV, 350 mV and 300 mV, respectively, as shown in Fig. 2d. The decreasing onset-potential shift with increasing STO thickness may be explainable as a consequence of a slightly increased Si suboxide formation with increasing STO thickness, which would increase the voltage drop across the oxide layer.

PEC performance

Devices with four unit cells of STO on p-Si and a 1 μm diameter Ti/Pt metal catalyst were used to examine the PEC performance in more detail. Figure 3a shows the LSV results and applied-bias photon-to-current efficiency (ABPE). An external bias (V_b) must be applied between the photoelectrode and counter electrode for small bandgap materials, such as Si, with the resulting ABPE given by:

$$\mathrm{ABPE} = \left(\frac{\left|j\left(\mathrm{mA\,cm^{-2}}\right)\right| \times \left(1.23 - \left|V_b\right|\right)(\mathrm{V})}{I\left(\mathrm{mW\,cm^{-2}}\right)}\right) \times 100\% \qquad (1)$$

where j is the photocurrent density, I the incident illumination intensity (100 mW cm^{-2} in this work) and V_b the potential versus ideal counter electrode. The ABPE calculated from measurements shown in Fig. 3a for the four-unit-cell STO on p-Si with a 1 μm diameter Ti/Pt catalyst is 2.9%.

Stability measurements were conducted using chronoamperometry at a fixed potential of 0 V versus Ag/AgCl. As shown in Fig. 3b, no degradation was observed after 35 hours of operation, which suggests a stable photocathode performance. Stability

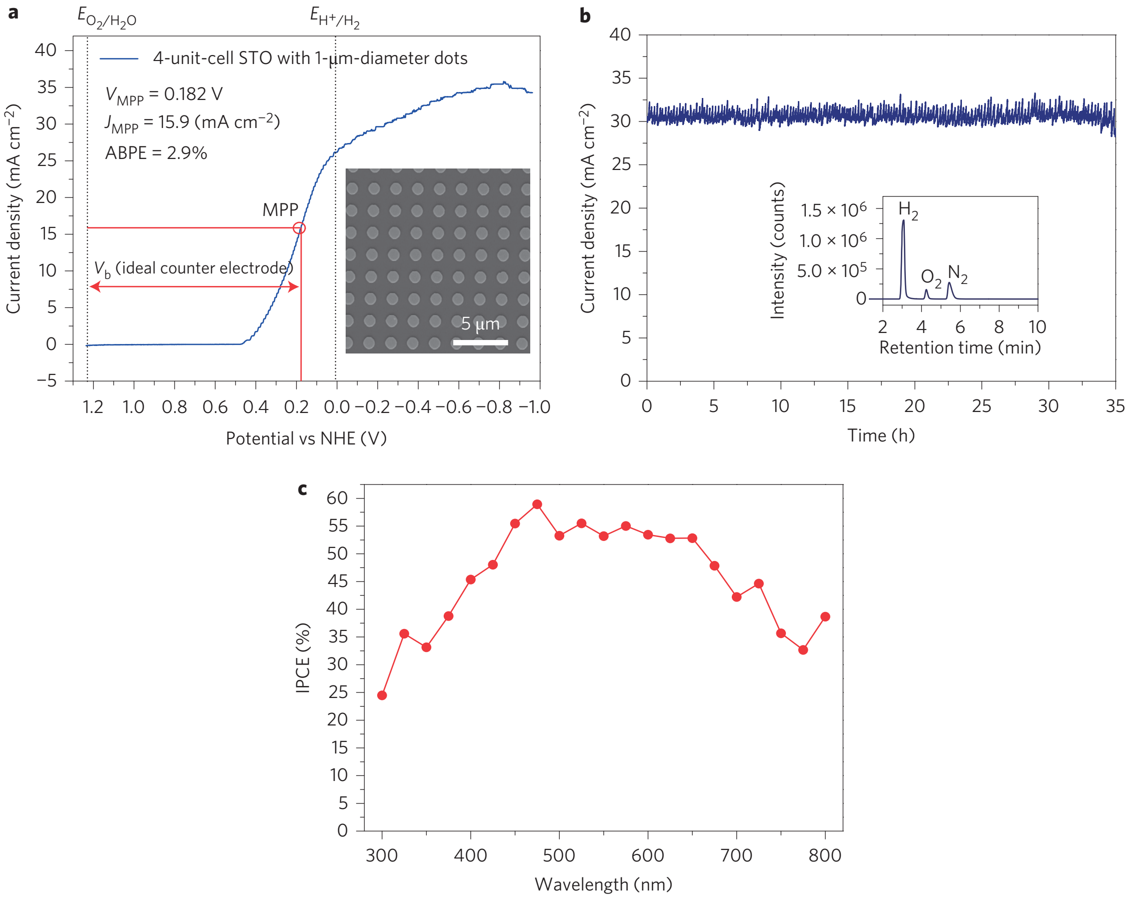

Figure 3 | PEC characterization and performance. **a**, LSV of a 20 nm Pt/30 nm Ti/four-unit-cell STO/p-Si(001) sample. The diameter and spacing of Pt/Ti dots are 1 µm and 2 µm, respectively, as shown in the inset top-view SEM image. **b**, Stability as indicated by the steady-state photocurrent characterization with a device held at 0 V versus Ag/AgCl under 100 mW cm^{-2} illumination in 0.5 M H_2SO_4. The inset is a gas chromatogram of the produced gas. **c**, Incident IPCE was measured at an applied potential of –0.4 V versus NHE using a xenon arc lamp equipped with a monochromator. MPP, maximum power point.

measurements for a bare p-Si wafer (with HF treatments to remove native oxide) are shown in Supplementary Fig. 5. The small fluctuation of photocurrent was caused by the produced H_2 bubbles coming off the photocathode surface. The inset in Fig. 3b shows a gas chromatography measurement of the gaseous product collected at the photocathode, which confirms H_2 production. A video is available in the Supplementary Information and shows H_2 and oxygen generation at the working and counter electrode, respectively.

The incident-photon-to-current conversion efficiency (IPCE) was also determined for this device and is given by:

$$\mathrm{IPCE} = \frac{1239.8\,(\mathrm{V\,nm}) \times \left|j\left(\mathrm{mA\,cm^{-2}}\right)\right|}{P_{\mathrm{mono}}\left(\mathrm{mW\,cm^{-2}}\right) \times \lambda\,(\mathrm{nm})} \tag{2}$$

where P_{mono} is the monochromated illumination power intensity and λ the wavelength. As illustrated in Fig. 3c, the shape of the IPCE curve accords well with that of traditional Si-based solar cells with an effective current response from 475 to 725 nm.

Metal catalyst patterning and size effects

Comparing LSV results for the four-unit-cell samples in Figs 2c and 3a, we found the performance was improved by decreasing the size of the metal catalyst, as also observed in previous work[3]. As the total thickness of the bilayer metal catalyst is 50 nm, light can only be absorbed by uncovered regions. Esposito *et al.* suggested that an inversion channel is formed underneath the oxide layer along which electrons can travel to an adjacent metal catalyst, as shown in Fig. 4a[3]. However, during long-distance travel in an inversion layer, electrons will suffer from electron–phonon scattering and electron–hole recombination. In addition, decreasing the ratio of the covered region to the exposed surface area enhances light absorption and performance. For these reasons, we explored nanosize metal catalysts to improve PEC performance.

Metal nanostructures can be fabricated in many ways. Electron-beam lithography can define nanostructures precisely but suffers from limited throughput and high cost. In nanocrystal non-volatile memory devices, nanocrystals are obtained by annealing a thin-film metal[43]. However, as discussed earlier, a 30 nm Ti layer with a 20 nm Pt layer is utilized for improved work function and performance of the MIS structure. It is difficult to create nanocrystals by annealing while retaining the bilayer metal structure. As an alternative method for metal-catalyst nanostructuring, we employed nanosphere lithography[44,45], an inexpensive, maskless process for submicron-scale structure fabrication that is compatible with bilayer metal deposition. The nanosphere lithography process flow for producing the Ti/Pt nanostructures is shown schematically in Fig. 4b. From left to right are nanosphere deposition (Langmuir–Blodgett method), metal deposition and nanosphere lift-off. A scanning electron microscope (SEM) image of the Ti/Pt-nanostructured surface is shown in Fig. 4b.

LSV results and a summary of the measurements for samples with different metal-catalyst sizes are presented in Fig. 4c and Table 1. The existence of an inversion layer underneath STO is confirmed by performing capacitance–voltage measurements under

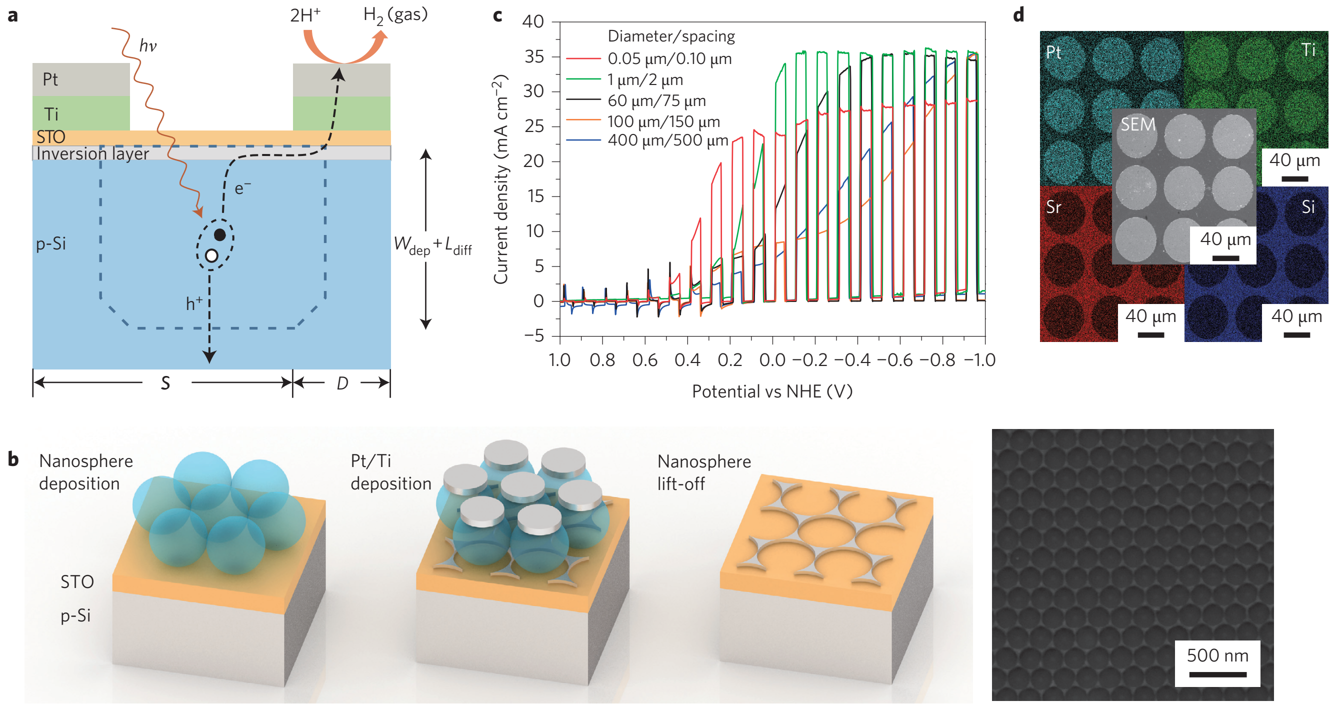

Figure 4 | Nanostructured metal-catalyst fabrication and performance. **a**, Schematic plot of the minority-carrier transport. **b**, Schematic of the nanosphere lithography process. From left to right are the nanosphere deposition, metal deposition and nanosphere lift-off. The final structure was characterized by SEM. **c**, LSV of a four-unit-cell 20 nm Pt/30 nm Ti/STO/p-Si(001) sample with various metal-catalyst feature sizes. **d**, Energy dispersive X-ray (EDX) image of a four-unit-cell sample with a 60 μm metal-catalyst feature size. The 60 μm feature-size sample was chosen because of the resolution limit of EDX.

Table 1 | Relationship between diameter and spacing (*D*/*S*), coverage factor and ABPE.

D/*S* (μm/μm)	Coverage ratio ($\pi D^2/4S^2$)	Maximum distance to metal catalyst (μm)	ABPE (%)
0.05/0.1	~0.196	0.1	4.9
1/2	0.196	1.8	2.9
60/75	0.5	46	1.25
100/200	0.196	183	1.23
400/500	0.5	307	0.78

dark and light conditions at various frequencies, as shown in Supplementary Fig. 4b. W_{dep} is the depletion width and L_{diff} is the diffusion length of electrons. In the p-Si substrate, we estimate $W_{dep} \approx 2$μm and $L_{diff} \approx 60$ μm for the wafer-doping concentration we used[46]. *D* and *S* represent the diameter and spacing of the metal catalyst, respectively, and L_t is the maximum distance an electron needs to travel to the nearest metal catalyst. For $L_t > L_{diff}$ (*D*/*S* of 100 μm/200 μm and 400 μm/500 μm), the efficiency is enhanced with a decreasing surface-coverage ratio because of the increased light absorption, as seen in Fig. 4c and Table 1. However, for feature sizes larger than 100 μm, the fill factor in the LSV measurements shown in Fig. 4c is very low for two reasons. First, for electrons that travel in the inversion layer, the large channel length introduces more electron–phonon scattering and recombination, which decreases the current density. Second, only some of the photogenerated electrons can be injected into the inversion layer. The rest of the electrons transport by diffusion within the bulk. This can be seen in samples with a *D*/*S* of 60 μm/75 μm. Although it has the same surface coverage ratio as the 400 μm/500 μm structure, the 60 μm/75 μm sample has a much higher fill factor compared with the 400 μm/500 μm sample because $L_t < L_{diff}$ for the 60 μm/75 μm sample. For $L_t < L_{diff}$, a smaller coverage ratio also yields a higher efficiency, as seen by comparing the 60 μm/75 μm with the 1 μm/2 μm sample. However, by observing the LSV for the 60 μm/75 μm, 100 μm/200 μm and 400 μm/500 μm samples, we found that they all present a kink around 0 V versus NHE, in which region the photocurrent density remains at a low level. This suggests that there must be another limiting factor. By comparing 0.05 μm/0.1 μm and 1 μm/2 μm samples, it was found that the ABPE doubled if $L_t \ll W_{dep}$. The origin of this phenomenon is currently unclear and further study is underway. The 0.05 μm/0.1 μm sample created by nanosphere lithography achieved a record-high 4.9% ABPE for water reduction in a single-junction Si photocathode[3,8,13], in which the photogenerated electrons only need to travel very short distances to the nearest metal catalyst. In addition, the short travel distances yield a reduced recombination rate in the depletion region, which results in an increase of V_{oc} to 0.6 V. The reduced maximum photocurrent density for the 0.05 μm/0.1 μm sample results from incomplete coverage of the device surface by the metal catalyst because of imperfection in the fabrication process for this range of feature sizes. Thus, we anticipate that further optimization of the fabrication-process flow may lead to additional improvements in performance.

Conclusions

We have demonstrated that the epitaxial STO/Si heterojunction is an efficient and stable photocathode for water splitting. A high photocurrent density (35 mA cm^{-2}), onset potential shift (450 mV) and long-term stability were achieved because of the single-crystalline nature of STO, lattice matching, crystalline-interface quality and negligible conduction-band offset between STO and Si. In addition, we extended our work to the relation between the size of the surface metal catalyst and efficiency. The results indicate that utilizing characteristic sizes smaller than the limiting factors (diffusion length and depletion width) would greatly increase the efficiency. Hence, sub-100 nm nanostructures made by nanosphere lithography yielded the highest reported ABPE efficiency of 4.9% for water reduction in a single-junction Si photocathode[3,4,13]. This finding is not limited to the STO/Si platform and should provide a general method for catalyst engineering.

Methods

MBE. This was used to grow crystalline STO directly on Si(001) using a variant of the Motorola-developed process[42]. The as-received Si(001) wafers were cut to 20×20 mm^2, then cleaned ultrasonically with acetone, isopropyl alcohol and deionized (DI) water for ten minutes each, followed by ultraviolet/ozone exposure for 15 minutes to remove residual carbon contamination. On loading into the MBE chamber (DCA 600), the native oxide was desorbed using a Sr-assisted deoxidation process[47]. After achieving a clean Si(001) surface with 2×1 reconstruction, a half monolayer of Sr metal was deposited on the Si substrate at 550 °C to form the 2×1 strontium silicide template layer.

To deposit the STO protective layer, the substrate was cooled to below 200 °C and molecular oxygen was slowly ramped from 5×10^{-8} torr to 2×10^{-7} torr over several minutes to ensure that the underlying Si was not oxidized during the initial STO deposition. Sr and Ti were co-deposited from effusion cells during oxygen ramping at a rate of one monolayer per minute to a thickness between four and ten unit cells of STO. Oxygen was then removed and the film was annealed for five minutes at 550 °C under vacuum to crystallize the STO layer. The crystalline structure was verified by *in situ* reflection RHEED using an electron energy of 21 keV at a glancing angle of ~3°.

XPS. This was performed *in situ* using a VG Scienta R3000 Analyzer and a monochromated Al Kα source at 1,486.6 eV to determine the film composition and verify the absence of SiO_x at the STO–Si interface. High-resolution spectra of the Sr 3*d*, Ti 2*p*, O 1*s*, C 1*s* and Si 2*p* core levels were measured using a pass energy of 100 eV with an analyser slit width of 0.4 mm. Each high-resolution scan was measured four times and summed, using 50 meV steps with a dwell time of 157 ms per step. Film composition was estimated using CasaXPS (ver. 2.3.16) peak fitting, in which the integrated intensities are divided by the Wagner relative-sensitivity factors after a Shirley background subtraction[48]. Additionally, a thickness-dependent energy exponent between 0 and 0.78 was used to account for the kinetic energy variation with sampling depth[49]. The maximum exponent value (0.78) was calibrated using an STO single-crystal substrate (MTI Corp.) for which the Sr:Ti ratio was assumed to be 1:1.

Lithography and metallization. After film growth and XPS analysis, the substrate was removed from the ultrahigh-vacuum system for deposition of the bilayer metal catalysts. Ordered metallic array catalysts were fabricated by lithographic patterning and a lift-off process. For photolithographic patterning, the photoresist (AZ 5209) was exposed and developed using standard methods. For nanosphere lithography, 200 nm diameter polystyrene nanospheres (Polysciences Inc.) and 18 MΩ DI water were used for the nanosphere mask preparation. The polystyrene nanosphere solution was dropped on top of microscope coverslips, which were then introduced to an air–water interface in a Petri dish filled with DI water. The monolayer was then transferred into the immersed substrate by lifting the substrate slightly. For metallization, Pt (99.99%, Alfa Aesar, USA) and Ti (99.99%, Alfa Aesar, USA) layers were then deposited onto the STO surface in an electron-beam evaporator (CHA Industries) with a base pressure of 1.0×10^{-6} torr. During the bilayer metal deposition, a vacuum was maintained to prevent oxidation of the Ti layer. The film thickness was monitored using a quartz-crystal monitor and the deposition rates were maintained at 1 Å s^{-1}. The back contact (3 nm Cr/100 nm Au) was formed using the same methods. Optical microscopy (Olympus, USA) and SEM (Zeiss, USA) were utilized to characterize the topography.

PEC measurements. PEC measurements were conducted using a CH660D potentiostat (CH Instruments, Austin, USA). A sulfuric acid electrolyte (0.5 M H_2SO_4) was used for all measurements, prepared from 18 MΩ DI water and concentrated (98%) sulfuric acid (Fisher Chemical, USA). Before measurement, the prepared electrolyte was purged by Ar for more than one hour. A xenon arc lamp was used as the light source and was calibrated to 100 mW cm^{-2}. A single-compartment PEC test cell was utilized. A Pt wire and Ag/AgCl/1M KCl electrode (CH Instruments, Austin, USA) served as the counter electrode and reference electrode, respectively. Incident-photon-to-photocurrent efficiency was measured using a xenon lamp equipped with a monochromator. The incident-light intensity versus wavelength was measured with a standard Si photodiode. In addition, no sacrificial reagent was used in all the PEC measurements.

Received 5 May 2014; accepted 22 October 2014;

References

1. Fujishima, A. & Honda, K. Electrochemical photolysis of water at a semiconductor electrode. *Nature* **238,** 37–38 (1972).
2. Lewis, N. S. *et al.* Solar water splitting cells. *Chem. Rev.* **110,** 6446–6473 (2010).
3. Esposito, D. V., Levin, I., Moffat, T. P. & Talin, A. A. H_2 evolution at Si-based metal–insulator–semiconductor photoelectrodes enhanced by inversion channel charge collection and H spillover. *Nature Mater.* **12,** 562–568 (2013).
4. Kye, J. *et al.* Platinum monolayer electrocatalyst on gold nanostructures on silicon for photoelectrochemical hydrogen evolution. *ACS Nano* **7,** 6017–6023 (2013).
5. Sun, K. *et al.* Nickel oxide functionalized silicon for efficient photo-oxidation of water. *Energy Environ. Sci.* **5,** 7872–7877 (2012).
6. Chen, Y. W. *et al.* Atomic layer-deposited tunnel oxide stabilizes silicon photoanodes for water oxidation. *Nature Mater.* **10,** 539–544 (2011).
7. Seger, B. *et al.* Hydrogen production using a molybdenum sulfide catalyst on a titanium-protected n plus p-silicon photocathode. *Angew. Chem. Int. Ed.* **51,** 9128–9131 (2012).
8. Seger, B. *et al.* Using TiO_2 as a conductive protective layer for photocathodic H_2 evolution. *J. Am. Chem. Soc.* **135,** 1057–1064 (2013).
9. Kenney, M. J. *et al.* High-performance silicon photoanodes passivated with ultrathin nickel films for water oxidation. *Science* **342,** 836–840 (2013).
10. Reece, S. Y. *et al.* Wireless solar water splitting using silicon-based semiconductors and earth-abundant catalysts. *Science* **334,** 645–648 (2011).
11. Pijpers, J. J. H. *et al.* Light-induced water oxidation at silicon electrodes functionalized with a cobalt oxygen-evolving catalyst. *Proc. Natl Acad. Sci. USA* **108,** 10056–10061 (2011).
12. Sun, K. *et al.* Metal oxide composite enabled nanotextured Si photoanode for efficient solar driven water oxidation. *Nano Lett.* **13,** 2064–2072 (2013).
13. Dasgupta, N. P. *et al.* Atomic layer deposition of platinum catalysts on nanowire surfaces for photoelectrochemical water reduction. *J. Am. Chem. Soc.* **135,** 12932–12935 (2013).
14. Paracchino, A. *et al.* Highly active oxide photocathode for photoelectrochemical water reduction. *Nature Mater.* **10,** 456–461 (2011).
15. Khan, S. U. M., Al-Shahry, M. & Ingler, W. B. Efficient photochemical water splitting by a chemically modified *n*-TiO_2. *Science* **297,** 2243–2245 (2002).
16. Chen, X. B., Liu, L., Yu, P. Y. & Mao, S. S. Increasing solar absorption for photocatalysis with black hydrogenated titanium dioxide nanocrystals. *Science* **331,** 746–750 (2011).
17. Warren, S. C. *et al.* Identifying champion nanostructures for solar water-splitting. *Nature Mater.* **12,** 842–849 (2013).
18. Shi, J. *et al.* Interface engineering by piezoelectric potential in ZnO-based photoelectrochemical anode. *Nano Lett.* **11,** 5587–5593 (2011).
19. McKone, J. R., Pieterick, A. P., Gray, H. B. & Lewis, N. S. Hydrogen evolution from Pt/Ru-coated p-type WSe_2 photocathodes. *J. Am. Chem. Soc.* **135,** 223–231 (2012).
20. Liao, L. *et al.* Efficient solar water-splitting using a nanocrystalline CoO photocatalyst. *Nature Nanotech.* **9,** 69–73 (2013).
21. Khaselev, O. & Turner, J. A. A monolithic photovoltaic–photoelectrochemical device for hydrogen production via water splitting. *Science* **280,** 425–427 (1998).
22. Li, Y. *et al.* Cobalt phosphate-modified barium-doped tantalum nitride nanorod photoanode with 1.5% solar energy conversion efficiency. *Nature Commun.* **4,** 2566 (2013).
23. Higashi, M., Domen, K. & Abe, R. Highly stable water splitting on oxynitride TaON photoanode system under visible light irradiation. *J. Am. Chem. Soc.* **134,** 6968–6971 (2012).
24. Li, Y. *et al.* Vertically aligned Ta_3N_5 nanorod arrays for solar-driven photoelectrochemical water splitting. *Adv. Mater.* **25,** 125–131 (2013).
25. Powell, D. M. *et al.* Crystalline silicon photovoltaics: a cost analysis framework for determining technology pathways to reach baseload electricity costs. *Energy Environ. Sci.* **5,** 5874–5883 (2012).
26. Swanson, R. M. A vision for crystalline silicon photovoltaics. *Prog. Photovoltaics Res. Appl.* **14,** 443–453 (2006).
27. Sim, U. *et al.* N-doped monolayer graphene catalyst on silicon photocathode for hydrogen production. *Energy Environ. Sci.* **6,** 3658–3664 (2013).
28. Wang, X. *et al.* High-performance silicon nanowire array photoelectrochemical solar cells through surface passivation and modification. *Angew. Chem. Int. Ed.* **50,** 9861–9865 (2011).
29. Munoz, E. C., Schrebler, R. S., Orellana, M. A. & Cordova, R. Rhenium electrodeposition process onto p-Si(100) and electrochemical behaviour of the hydrogen evolution reaction onto p-Si/Re/0.1 M H_2SO_4 interface. *J. Electroanal. Chem.* **611,** 35–42 (2007).
30. Strandwitz, N. C. *et al.* Photoelectrochemical behavior of n-type Si(100) electrodes coated with thin films of manganese oxide grown by atomic layer deposition. *J. Phys. Chem. C* **117,** 4931–4936 (2013).
31. Lana-Villarreal, T., Straboni, A., Pichon, L. & Alonso-Vante, N. Photoelectrochemical characterization of p-type silicon electrodes covered with tunnelling nitride dielectric films. *Thin Solid Films* **515,** 7376–7381 (2007).
32. McKee, R. A., Walker, F. J. & Chisholm, M. F. Crystalline oxides on silicon: the first five monolayers. *Phys. Rev. Lett.* **81,** 3014–3017 (1998).
33. Yu, Z. *et al.* Advances in heteroepitaxy of oxides on silicon. *Thin Solid Films* **462–463,** 51–56 (2004).
34. Warusawithana, M. P. *et al.* A ferroelectric oxide made directly on silicon. *Science* **324,** 367–370 (2009).
35. Demkov, A. A. *et al.* Monolithic integration of oxides on semiconductors. *ECS Transactions* **54,** 255–269 (2013).

36. McKee, R. A., Walker, F. J. & Chisholm, M. F. Physical structure and inversion charge at a semiconductor interface with a crystalline oxide. *Science* **293,** 468–471 (2001).
37. Chambers, S. A. *et al.* Band discontinuities at epitaxial $SrTiO_3$/Si(001) heterojunctions. *Appl. Phys. Lett.* **77,** 1662–1664 (2000).
38. Chambers, S. *et al.* Band offset and structure of $SrTiO_3$/Si(001) heterojunctions. *J. Vac. Sci. Technol. A* **19,** 934–939 (2001).
39. Zhang, X. *et al.* Atomic and electronic structure of the Si/$SrTiO_3$ interface. *Phys. Rev. B* **68,** 125323 (2003).
40. Amy, F. *et al.* Band offsets at heterojunctions between $SrTiO_3$ and $BaTiO_3$ and Si(100). *J. Appl. Phys.* **96,** 1635–1639 (2004).
41. Robertson, J. Band offsets of wide-band-gap oxides and implications for future electronic devices. *J. Vac. Sci. Technol. B* **18,** 1785–1791 (2000).
42. Yu, Z. *et al.* Epitaxial perovskite thin films grown on silicon by molecular beam epitaxy. *J. Vac. Sci. Technol. B* **18,** 1653–1657 (2000).
43. Chang, T. C., Jian, F. Y., Chen, S. C. & Tsai, Y. T. Developments in nanocrystal memory. *Mater. Today* **14,** 608–615 (2011).
44. Haynes, C. L. & Van Duyne, R. P. Nanosphere lithography: a versatile nanofabrication tool for studies of size-dependent nanoparticle optics. *J. Phys. Chem. B* **105,** 5599–5611 (2001).
45. Hsu, C. M., Connor, S. T., Tang, M. X. & Cui, Y. Wafer-scale silicon nanopillars and nanocones by Langmuir–Blodgett assembly and etching. *Appl. Phys. Lett.* **93,** 133109 (2008).
46. Sze, S. M. & Ng, K. K. *Physics of Semiconductor Devices* (Wiley, 2006).
47. Wei, Y. *et al.* Mechanism of cleaning Si(100) surface using Sr or SrO for the growth of crystalline $SrTiO_3$ films. *J. Vac. Sci. Technol. B* **20,** 1402–1405 (2002).
48. Wagner, C. D. Sensitivity factors for XPS analysis of surface atoms. *J. Electron Spectrosc.* **32,** 99–102 (1983).
49. Wagner, C. D., Davis, L. E. & Riggs, W. M. The energy dependence of the electron mean free path. *Surf. Interface Anal.* **2,** 53–55 (1980).

Acknowledgements

The authors acknowledge research support from the National Science Foundation (ECCS-1120823 and Award DMR-1207342), the Office of Naval Research (Grant N00014-10-10489) and the Judson S. Swearingen Regents Chair in Engineering at the University of Texas at Austin.

Author contributions

L.J., M.D.M., J.G.E. and E.T.Y. contributed to the design concept. L.J., X.L., S.W. and H.H. performed the fabrication process and measurements. M.D.M., A.B.P., A.A.D. and J.G.E. performed the MBE growth. All authors discussed the results and commented on the manuscript.

Additional information

Supplementary information is available in the online version of the paper. Reprints and permissions information is available online at www.nature.com/reprints. Correspondence and requests for materials should be addressed to L.J.

Competing financial interests

The authors declare no competing financial interests.